Electrochemically Mediated Atom Transfer Radical Polymerization

Andrew J. D. Magenau, *et al.*

Science **332**, 81 (2011);
DOI: 10.1126/science.1202357

doped semiconductors relates to distortions of the crystal structure by the dopants leading to band-tailing and a red shift of the gap. To address the role of band-tailing we employed an atomistic treatment of the electronic structure of the QD, where disorder was introduced by randomly displacing In or As atoms (*26*). Band-tailing occurs mainly for the valence band edge as evident from the DOS shown in Fig. 4E for different impurity numbers. This results from the heavier effective mass and the denser level structure of the valence band, compared to the light effective mass of the highly delocalized electron. From the DOS we estimate the shifts in the band gaps induced by disorder as shown in Fig. 4F. Tailing occurs for distortions to the In atoms, As atoms, both atoms or only surface atoms. The band gap decreases for higher dopant concentrations. Note that the As distortions lead to larger shifts, consistent with its larger ionic radii.

In Fig. 4, G and H, we show the calculated and measured shifts (for Ag impurities) for several QD sizes as a function of the dopant concentration, respectively. The striking similarities between the theory and experiments suggest that the spectral shifts observed in Ag, unlike the case of Cu, are dominated by band-tailing, although clearly in both cases there is an interplay between band tailing and the impurity band formation. Both theory and experiments show a rapid increase in the magnitude of the shift, reaching a plateau at high dopant concentrations. The increase in the shift depends on the level of disorder induced by each dopant. Furthermore, the shifts decrease with increasing QD size in both cases. We note that in Cu, although a contribution of band-tailing is also possible, the band-filling effect discussed above dominates, leading to the blue shift in that case.

Doping semiconductor NCs with metal impurities provides further means to control their optical and electronic properties. We developed a synthesis for n- and p-type doped InAs NCs by introducing Cu and Ag impurities, respectively. Cu-doped particles showed a blue shift in the absorption with only small bleaching. This is in line with the increased DOS, which results from the addition of new impurity levels that develop into an impurity band, and their partial filling with electrons from interstitial Cu impurities. Correspondingly, the STS measurements show a shift in the Fermi energy to near the conduction band edge, and the development of a confined impurity band. This behavior was rationalized by a TB model, and its size dependence indicates that the confinement leads to localization of the impurity states in small NCs. Conversely, STS measurements of Ag-doped NCs led to a shift of the Fermi energy toward the valence band, proving p-type doping. This was accompanied by a red shift of both absorption and emission peaks, attributed to band-tailing effects analogous to the Urbach tail, in line with Ag adopting substitutional sites. The magnitude and size dependence of the band narrowing agree with atomistic electronic structure calculations incorporating structural disorder induced by the dopants. Interestingly, introduction of Au impurities as a substitutional dopant, although broadening the STS spectra, maintains the position of the Fermi level and does not lead to spectral shifts, in line with its isovalent nature with In. The controlled ability to synthesize n- and p-type doped NCs, along with better understanding of the heavily doped impurity regime in colloidal QDs, opens avenues for diverse electronic and optoelectronic devices.

References and Notes

1. S. M. Sze, *Physics of Semiconductor Devices* (Wiley-Interscience, New York, ed. 2, 1981).
2. S. Coe, W.-K. Woo, M. Bawendi, V. Bulović, *Nature* **420**, 800 (2002).
3. I. Gur, N. A. Fromer, M. L. Geier, A. P. Alivisatos, *Science* **310**, 462 (2005).
4. D. V. Talapin, C. B. Murray, *Science* **310**, 86 (2005).
5. D. J. Norris, A. L. Efros, S. C. Erwin, *Science* **319**, 1776 (2008).
6. D. Turnbull, *J. Appl. Phys.* **21**, 1022 (1950).
7. G. M. Dalpian, J. R. Chelikowsky, *Phys. Rev. Lett.* **96**, 226802 (2006).
8. T. L. Chan, M. L. Tiago, E. Kaxiras, J. R. Chelikowsky, *Nano Lett.* **8**, 596 (2008).
9. M. Shim, P. Guyot-Sionnest, *Nature* **407**, 981 (2000).
10. C. Wang, M. Shim, P. Guyot-Sionnest, *Science* **291**, 2390 (2001).
11. D. Yu, C. J. Wang, P. Guyot-Sionnest, *Science* **300**, 1277 (2003).
12. N. Pradhan, D. Goorskey, J. Thessing, X. Peng, *J. Am. Chem. Soc.* **127**, 17586 (2005).
13. R. N. Bhargava, D. Gallagher, X. Hong, A. Nurmikko, *Phys. Rev. Lett.* **72**, 416 (1994).
14. C. A. Stowell, R. J. Wiacek, A. E. Saunders, B. A. Korgel, *Nano Lett.* **3**, 1441 (2003).
15. S. C. Erwin *et al.*, *Nature* **436**, 91 (2005).
16. Y. Yang, O. Chen, A. Angerhofer, Y. C. Cao, *J. Am. Chem. Soc.* **128**, 12428 (2006).
17. C. Tuinenga, J. Jasinski, T. Iwamoto, V. Chikan, *ACS Nano* **2**, 1411 (2008).
18. S. Roy *et al.*, *J. Phys. Chem. C* **113**, 13008 (2009).
19. R. Xie, X. Peng, *J. Am. Chem. Soc.* **131**, 10645 (2009).
20. R. A. Abram, G. J. Rees, B. L. H. Wilson, *Adv. Phys.* **27**, 799 (1978).
21. J. Tauc, Ed., *Amorphous and Liquid Semiconductors* (Plenum, London, 1976).
22. N. Porras-Montenegro, S. T. Perez-Merchancano, A. Latge, *J. Appl. Phys.* **74**, 7624 (1993).
23. S.-S. Li, J.-B. Xia, *J. Appl. Phys.* **101**, 093716 (2007).
24. M. Barati, G. Rezaei, M. R. K. Vahdani, *Phys. Status Solidi* **244**, 2605 (2007) (b).
25. T. Mokari, A. Aharoni, I. Popov, U. Banin, *Angew. Chem. Int. Ed.* **45**, 8001 (2006).
26. See supporting material on *Science* Online.
27. U. Banin, O. Millo, *Annu. Rev. Phys. Chem.* **54**, 465 (2003).
28. K. S. Leschkies, M. S. Kang, E. S. Aydil, D. J. Norris, *J. Phys. Chem. C* **114**, 9988 (2010).
29. J. Dixon, D. Enright, *J. Appl. Phys.* **30**, 753 (1959).
30. B. Tuck, P. R. Jay, *J. Phys. D* **11**, 1413 (1978).
31. D. V. Melnikov, J. R. Chelikowsky, *Phys. Rev. Lett.* **92**, 046802 (2004).

32. We thank the staff of the Unit for Nanocharacterization of the Center for Nanoscience and Nanotechnology in the Hebrew University, Jerusalem, headed by I. Popov, as well as V. Gutkin for help in the XPS studies. Supported by a grant from the European Research Council under the European Community's Seventh Framework Programme (FP7/2007-2013)/ERC grant agreement 203413 (U.B.); the Israel Science Foundation (O.M.); Seventh Framework Programme Marie Curie International Outgoing Fellowships for Career Development project Hierarchical Junction Solar Cells (E.R.); the Harry de Jur Chair in Applied Science (O.M.); the Alfred and Erica Larisch Memorial Chair (U.B.); an Azrieli Foundation fellowship (G.C.); and the Centre for Scientific Absorption, Ministry of Absorption, State of Israel (D.M.).

Supporting Online Material

www.sciencemag.org/cgi/content/full/332/6025/77/DC1
Materials and Methods
Figs. S1 to S24
Table S1
References

10 August 2010; accepted 10 February 2011
10.1126/science.1196321

Electrochemically Mediated Atom Transfer Radical Polymerization

Andrew J. D. Magenau,[1] Nicholas C. Strandwitz,[2] Armando Gennaro,[3] Krzysztof Matyjaszewski[1]*

Atom transfer radical polymerization is a versatile technique for exerting precise control over polymer molecular weights, molecular weight distributions, and complex architectures. Here, we show that an externally applied electrochemical potential can reversibly activate the copper catalyst for this process by a one-electron reduction of an initially added air-stable cupric species (Cu^{II}/Ligand). Modulation of polymerization kinetics is thereby tunable in real time by varying the magnitude of applied potential. Application of multistep intermittent potentials successfully triggers initiation of polymerization and subsequently toggles the polymerization between dormant and active states in a living manner. Catalyst concentrations down to 50 parts per million are demonstrated to maintain polymerization control manifested in linear first-order kinetics, a linear increase in polymer molecular weight with monomer conversion, and narrow polymer molecular weight distributions over a range of applied potentials.

Living polymerizations, introduced in 1956 by Szwarc (*1*), proceed in the absence of chain termination and chain transfer events, while concurrently maintaining instantaneous initiation and uniform growth of each propagating species (*2*). Processes of this nature allow

macromolecules to be prepared with precisely controlled molecular weights (M_n) and narrow molecular weight distributions (M_w/M_n). Polymerizations with living characteristics grant access to complex polymeric architectures and associated functionalities traditionally accessible only through ionic mechanisms. Relative to ionic polymerizations, radical pathways provide improved tolerance to functional groups and impurities, an expanded range of polymerizable monomers, and an efficient means of copolymerizing a variety of monomers (*3*, *4*). Controlled/living radical polymerizations (CRP), once thought unobtainable (*5*), have now been realized through many remarkable breakthroughs providing characteristics inherent to living polymerizations (*6*–*10*). Control is established in CRP by dynamic equilibria, either through dormant/active chain ends or degenerative transfer, essentially minimizing the concentration of propagating centers and concomitantly reducing bimolecular termination reactions occurring at diffusion-controlled reaction rates (*5*).

Real-time dynamic modulation of polymerization processes offers intermittent regulation of system variables that may include, but are not limited to, alterations of stereoselectivity (*11*), reactivity (*12*), and reaction rates (*13*–*16*). Variable polymerization rates have been demonstrated in only a few accounts using allosteric supramolecular catalysis (*13*), redox controlled catalysts (*14*), and temporal photoirradiation (*15*, *16*). These strategies require complex catalytic systems or are limited in their available tunable parameters. Furthermore, among the stimuli (e.g., light, pressure, and pH) available to externally influence polymerization behavior (*12*, *15*, *17*), application of an electrochemical stimulus (i.e., electrolysis) can be conveniently paired with atom transfer radical polymerization (ATRP), owing to the inherent redox-active nature of the ATRP catalytic system (*18*, *19*).

ATRP, one of the most powerful CRP techniques, proceeds through a concerted atom transfer mechanism via an inner-sphere electron-transfer process (*20*, *21*). The versatility of this process is exemplified by the vast array of suitable polymerization media, encompassing homogenous, heterogeneous, and aqueous systems (*3*, *22*–*25*), and attainable complex polymeric architectures (*3*, *26*). ATRP is dictated by an active/dormant equilibrium, shown in part by Fig. 1A, between lower oxidation state activators {i.e., $Cu^{I}Br$/tris[2-(dimethylamino)ethyl]amine ($Cu^{I}Br/Me_6TREN$)} and alkyl halides (P_n-Br), and their corresponding higher oxidation state deactivators (i.e., $Cu^{II}Br_2/Me_6TREN$) and radicals ($P_n^{\bullet}$), which are capable of monomer (M) addition (*3*, *4*, *6*, *10*). Establishing this dynamic equilibrium ($K_{ATRP} = k_a/k_{da}$), which strongly favors the dormant state, effectively decreases the concentration of propagating species and mediates the polymerization, allowing simultaneous growth of each polymeric chain.

In recent years, the ATRP process has been expanded via activators generated by electron transfer (AGET), a catalytic activation technique that reduces air-stable deactivators to their respective activators in situ by means of reducing agents (e.g., ascorbic acid, tin (II) 2-ethylhexanoate, and Cu^0) (*23*). AGET ATRP led to further process refinements by providing protocols with diminished $Cu^{II}X_2$ catalyst concentrations down to 10 parts per million (ppm) and simplified reaction setups in the presence of oxygen through activators regenerated by electron transfer (ARGET) and initiators for continuous activator regeneration (ICAR) ATRP (*27*–*29*). These systems are conducted in the presence of excess reducing agent where $Cu^{I}X$ activators are continuously regenerated from the $Cu^{II}X_2$ deactivators, a by-product of unavoidable termination events. Notably, the absolute concentration of copper catalyst can be decreased tremendously without affecting the polymerization rate, provided that an adequate $[Cu^{I}X/L]/[Cu^{II}X_2/L]$ ratio is sustained.

This report demonstrates the dynamic modulation of polymerization rates through electrochemical means, fostering precise temporal control over initiation, cessation, and rejuvenation of a CRP process. Electrochemical methods offer adjustable parameters (e.g., current, potential, and total charge passed) to manipulate polymerization rates and selective targeting of redox-active catalytic species. Moreover, advantages of ARGET ATRP such as ppm concentrations of catalyst (*27*, *30*) and tolerance to limited O_2 (*28*) are maintained and bolstered by elimination of environmentally less friendly chemical reducing agents and catalyst removal through electrodeposition (*31*). The proposed mechanism of ATRP mediated electrochemically (*e*ATRP) by (re)generation of activators is shown in Fig. 1A. Air-stable $Cu^{II}Br_2/Me_6TREN$ deactivator is reduced to $Cu^{I}Br/Me_6TREN$ activator electrochemically to invoke or trigger polymerization. In the absence of mass transport limitations, the extent of reduction is dictated by the applied potential (E_{app}), allowing a predefined $[Cu^{I}X/L]/[Cu^{II}X_2/L]$ ratio and fine-tuning of the polymerization rate. Further to this point, electrochemical methods allow a lower oxidation state catalyst ($Cu^{I}Br/Me_6TREN$) to be reverted back to its original higher oxidation deactivator state by simply shifting E_{app} to more positive values, thus providing a means to deactivate an ongoing polymerization.

Reduction of the $Cu^{II}Br_2/Me_6TREN$ complex was accomplished by application of a cathodic current (*32*). A similar methodology, although for generation of acutely air-sensitive click chemistry catalysts, was previously implemented for bioconjugation reactions with an isosahedral virus, resulting in high-efficiency reactions in the presence of ambient O_2 without chemical reducing agents (*33*). Before our electrolysis experiments, cyclic voltammograms (CVs) of methyl acrylate (MA) and acetonitrile (MeCN) over a potential range of 1.5 volts, from 0.0 to –1.5 V versus Ag^+/Ag were acquired to ensure the absence

[1]Center for Macromolecular Engineering, Department of Chemistry, Carnegie Mellon University, 4400 Fifth Avenue, Pittsburgh, PA 15213, USA. [2]Kavli Nanoscience Institute and Beckman Institute, and Division of Chemistry and Chemical Engineering, 210 Noyes Laboratory 127-72, California Institute of Technology, Pasadena, CA 91125, USA. [3]Department of Chemical Sciences, University of Padova, via Marzolo 1, 35131 Padova, Italy.

*To whom correspondence should be addressed. E-mail: km3b@andrew.cmu.edu

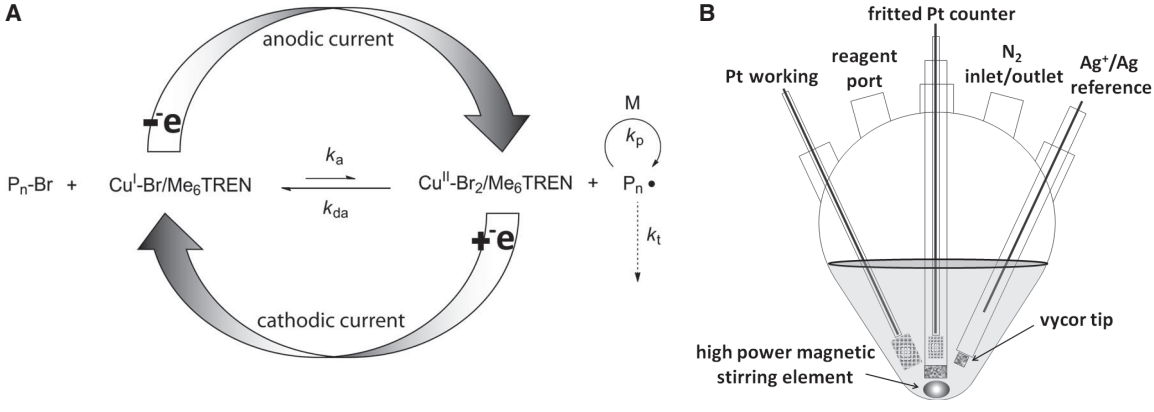

Fig. 1. (**A**) Mechanism of electrochemically mediated ATRP (*e*ATRP) under a cathodic current to (re)generate the $Cu^{I}Br_2/Me_6TREN$ complex and optional anodic current to revert to the $Cu^{II}Br_2/Me_6TREN$ complex for cessation of polymerization. (**B**) Electrolysis cell configured with platinum mesh working and counter electrodes. The two-compartment cell with a frit-separated counter electrode was maintained under an N_2 atmosphere at 25°C. Redox reactions of Cu^{II}/Cu^{I} couple were performed with applied potentials varied between –0.72 and –0.40 V versus an Ag^+/Ag reference electrode.

of any redox process that might interfere with the catalyst reduction (fig. S1A). After confirming the stability of the reaction medium, we acquired an additional CV in the presence of added $Cu^{II}Br_2$/Me_6TREN to identify the potential window appropriate for accurate manipulation of the oxidation states of our redox-active catalyst in electrolysis experiments. The copper catalyst couple (Cu^{II}/Cu^{I}) was observed to have an $E_{1/2}$ = –0.69 V versus Ag^+/Ag (–0.77 V versus Fc^+/Fc) (fig. S1B). Upon addition of the alkyl halide initiator, the CV changed due to regeneration of $Cu^{II}Br_2$/Me_6TREN by reaction of the electro-generated $Cu^{I}Br_2$/Me_6TREN complex with ethyl 2-bromopropionate (EBP) (fig. S1B). This process is similar to homogeneous redox catalysis (*34*): The $Cu^{I}Br_2$/Me_6TREN generated at the electrode reacts in solution to reduce EBP; a portion of the $Cu^{II}Br_2$/Me_6TREN thus regenerated returns to the electrode to be reduced again. The cathodic current is thereby enhanced, because reduction involves more than one-electron/molecule, whereas the anodic current decreases, because $Cu^{I}Br_2$/Me_6TREN is partially oxidized in solution.

Electrolysis of $Cu^{II}Br_2$/Me_6TREN was then carried out over a range of 60 mV, between –0.66 and –0.72 V, designed to probe the influence of applied potential (E_{app}). The cell was filled with ~12 mL of a 1:1 MA/MeCN (v/v) mixture containing 0.1 M electrolyte formulated with the following molar ratios $[MA]_0$:$[EBP]_0$:$[Me_6TREN]_0$:$[Cu^{II}Br_2]_0$ = 500:1:0.025:0.025. Electrolysis studies were carried out in a two-compartment cell fitted with platinum mesh working and counter electrodes, and a silver ion/silver (Ag^+/Ag) reference electrode, as illustrated in Fig. 1B. The counter electrode was always separated by a glass frit from the working electrode compartment, where polymerization occurs, to avoid oxidation of Cu^{I} and/or contamination of the working solution by oxidation products arising from the anodic process. An inert atmosphere and rapid stirring were maintained for the reaction duration to ensure stability of the $Cu^{I}Br$/Me_6TREN catalyst and adequate mass transport to the working electrode. Upon application of a –0.69 V potential, which corresponds to the $E_{1/2}$ of the Cu^{II}/Cu^{I} couple, rapid consumption of monomer occurred, reaching nearly 80% conversion within 2 hours (Fig. 2A). Linear first-order kinetic behavior was observed during the polymerization, indicating a constant concentration of propagating species (fig. S2), and an excellent correlation persisted between theoretical and experimental molecular weight values as the polymerization progressed (Fig. 2B). Molecular weight values increased linearly with conversion, and molecular weight distributions decreased gradually with increasing monomer conversion, reaching a minimum value of approximately M_w/M_n = 1.06. Furthermore, gel permeation chromatography (GPC) depicted monomodal distributions of polymeric species and a clear shift to larger molecular weight values with increasing conversion (Fig. 3).

The rate of ATRP is defined by the ratio of [$Cu^{I}Br_2$/Me_6TREN] and [$Cu^{II}Br_2$/Me_6TREN] and therefore depends on the extent to which $Cu^{II}Br_2$/Me_6TREN is reduced and consequently the E_{app} (*3*). Two additional and separate polymerizations were conducted with a 30-mV increase or decrease of the E_{app} to –0.72 and –0.66 V, respectively. An enhanced polymerization rate was observed at more negative potentials, whereas more positive potentials provided a slower rate of polymerization (Fig. 2A). Initial slopes in the first-order kinetic plots revealed an approximate rate enhancement by a factor of 2.4 by adjusting the E_{app} from –0.66 V to –0.72 V (fig. S2). In all cases, similar correlations between theoretical and experimental molecular weights were observed, and narrow molecular weight distributions were maintained even with enhanced polymerization rates (Fig. 2B and figs. S3 and S4).

Feasibility of an electrochemical switch to modulate copper oxidation states in situ, and thereby activate or deactivate polymerization, was demonstrated by repetitive stepping of the E_{app} from –0.69 V to –0.40 V. The first of these potentials favors formation of Cu^{I} at the electrode and hence triggers an active state, whereas the second potential, being more positive than $E_{1/2}$, favors Cu^{II} and leads to a dormant state. In the first hour of polymerization, no potential was applied and as a result no monomer conversion occurred, confirming the necessity of an E_{app} to trigger polymerization (Fig. 4A). Upon switching the potential to –0.69 V, 10% monomer conversion was observed after ~24 min, at which point the potential was switched to –0.40 V. Once this potential change occurred, the polymerization slowed and then halted, achieving ~2% monomer conversion in the first 25 min and a negligible amount over the following 20 min. The response time for deactivation was on average ≤20 min, whereas a polymerization could be revived in less than 15 min in the early stage of polymerization. This potential cycle was then repeated for three additional cycles, resulting in an increased monomer conversion to 28, 44, and then to 62% during active periods. This behavior manifests characteristics of a living polymerization with regard to efficient reinitiation of chain ends, owing to the preserved chain-end functionality. Throughout the cycling process, molecular weight values correlated strongly with their theoretically predetermined values, and low M_w/M_n values were maintained (Fig. 4B). Clustering of data points in the dormant periods is visible in Fig. 4B, whereas the molecular weight was shown to increase progressively with conversion during active periods when a sufficient E_{app} was imposed. Clear shifts to higher molecular weight were observed by GPC (fig. S5) without any substantial lower molecular weight fraction, confirming near quantitative reinitiation of poly(methyl acrylate) halogen chain ends.

Thus, we demonstrated a successful and well-controlled *e*ATRP of MA in MeCN. The *e*ATRP system is currently being extended to a larger range of monomers, media, and synthesis of various copolymers with complex architectures.

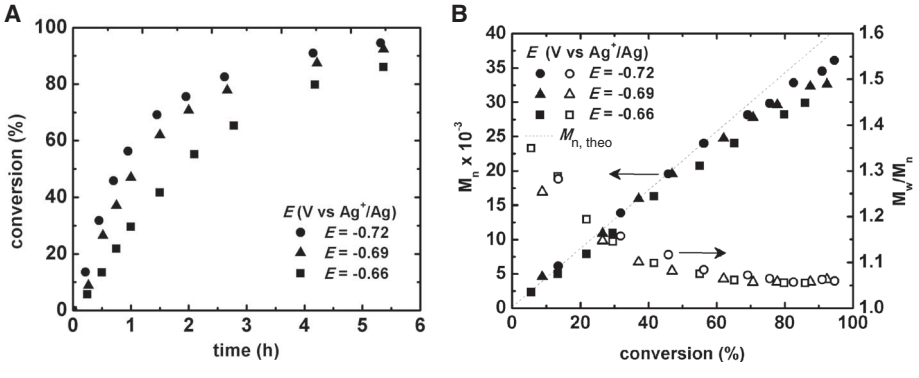

Fig. 2. (**A**) Monomer conversion with respect to time and (**B**) number average molecular weight (M_n) and M_w/M_n (where M_w is weight average molecular weight) with respect to conversion as a function of applied potential. Polymerizations were conducted in 50% (v/v) MA in MeCN at 25°C, with a total reaction volume of ~12 mL. $[MA]_0$ = 5.55 M; $[MA]_0$:$[EBP]_0$:$[Me_6TREN]_0$:$[Cu^{II}Br_2]_0$ = 500:1:0.025:0.025.

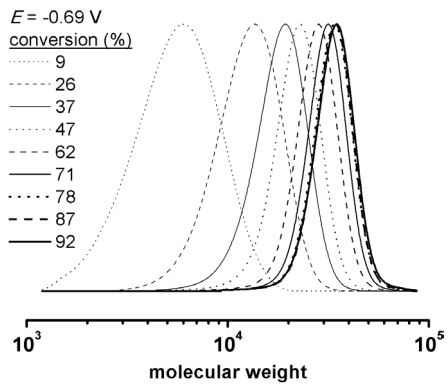

Fig. 3. Evolution of molecular weight with monomer conversion at –0.69 V versus Ag^+/Ag, measured by gel permeation chromatography.

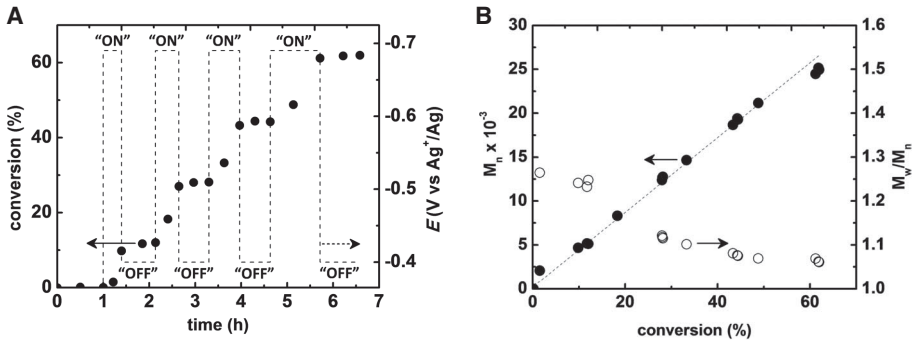

Fig. 4. (**A**) Conversion (solid circles) and applied potential (dashed line) with respect to time and (**B**) M_n and M_w/M_n with respect to conversion. Toggling between active and dormant states is represented by changes of the E_{app} values between −0.69V and −0.40 V versus Ag^+/Ag, respectively. Reaction conditions are identical to those stated in Fig. 2.

References and Notes

1. M. Szwarc, *Nature* **178**, 1168 (1956).
2. A. H. E. Müller, K. Matyjaszewski, *Controlled and Living Polymerizations: Methods and Materials* (Wiley-VCH, Weinheim, Germany, 2009).
3. K. Matyjaszewski, J. Xia, *Chem. Rev.* **101**, 2921 (2001).
4. M. Kamigaito, T. Ando, M. Sawamoto, *Chem. Rev.* **101**, 3689 (2001).
5. K. Matyjaszewski, T. P. Davis, *Handbook of Radical Polymerization*. (Wiley-Interscience, Hoboken, NJ, 2002).
6. T. E. Patten, J. Xia, T. Abernathy, K. Matyjaszewski, *Science* **272**, 866 (1996).
7. M. K. Georges, R. P. N. Veregin, P. M. Kazmaier, G. K. Hamer, *Macromolecules* **26**, 2987 (1993).
8. M. Kato, M. Kamigaito, M. Sawamoto, T. Higashimura, *Macromolecules* **28**, 1721 (1995).
9. J. Chiefari *et al.*, *Macromolecules* **31**, 5559 (1998).
10. J.-S. Wang, K. Matyjaszewski, *J. Am. Chem. Soc.* **117**, 5614 (1995).
11. L. H. Peeck, S. Leuthausser, H. Plenio, *Organometallics* **29**, 4339 (2010).
12. M. Benaglia *et al.*, *J. Am. Chem. Soc.* **131**, 6914 (2009).
13. H. J. Yoon, J. Kuwabara, J.-H. Kim, C. A. Mirkin, *Science* **330**, 66 (2010).
14. C. K. A. Gregson *et al.*, *J. Am. Chem. Soc.* **128**, 7410 (2006).
15. Y. Kwak, K. Matyjaszewski, *Macromolecules* **43**, 5180 (2010).
16. M. Tanabe *et al.*, *Nat. Mater.* **5**, 467 (2006).
17. J. Rzayev, J. Penelle, *Angew. Chem. Int. Ed.* **43**, 1691 (2004).
18. V. Bonometti, E. Labbé, O. Buriez, P. Mussini, C. Amatore, *J. Electroanal. Chem.* **633**, 99 (2009).
19. J. Qiu, K. Matyjaszewski, L. Thouin, C. Amatore, *Macromol. Chem. Phys.* **201**, 1625 (2000).
20. C. Y. Lin, M. L. Coote, A. Gennaro, K. Matyjaszewski, *J. Am. Chem. Soc.* **130**, 12762 (2008).
21. A. A. Isse *et al.*, *J. Am. Chem. Soc.*, ASAP (2011); doi: 10.1021/ja110538b.
22. W. A. Braunecker, K. Matyjaszewski, *Prog. Polym. Sci.* **32**, 93 (2007).
23. K. Min, H. Gao, K. Matyjaszewski, *J. Am. Chem. Soc.* **127**, 3825 (2005).
24. M. F. Cunningham, *Prog. Polym. Sci.* **33**, 365 (2008).
25. K. Min, K. Matyjaszewski, *Cent. Eur. J. Chem.* **7**, 657 (2009).
26. K. Matyjaszewski, N. V. Tsarevsky, *Nat. Chem.* **1**, 276 (2009).
27. K. Matyjaszewski *et al.*, *Proc. Natl. Acad. Sci. U.S.A.* **103**, 15309 (2006).
28. K. Matyjaszewski, H. Dong, W. Jakubowski, J. Pietrasik, A. Kusumo, *Langmuir* **23**, 4528 (2007).
29. W. Jakubowski, K. Matyjaszewski, *Angew. Chem.* **118**, 4594 (2006).
30. T. Pintauer, K. Matyjaszewski, *Chem. Soc. Rev.* **37**, 1087 (2008).
31. M. Nasser-Eddine, C. Delaite, P. Dumas, R. Vataj, A. Louati, *Macromol. Mater. Eng.* **289**, 204 (2004).
32. Materials and methods are available as supporting material on *Science* Online.
33. V. Hong, A. K. Udit, R. A. Evans, M. G. Finn, *ChemBioChem* **9**, 1481 (2008).
34. A. A. Isse, A. Gennaro, *J. Phys. Chem. A* **108**, 4180 (2004).

35. We acknowledge the U.S. National Science Foundation (grants DMR 09-69301 and CHE 10-26060) and the members of the CRP Consortium at Carnegie Mellon University for financial support. N.C.S. acknowledges the U.S. National Science Foundation for an American Competitiveness in Chemistry postdoctoral fellowship (CHE-1042006). A.J.D.M. and K.M. filed a U.S. provisional patent application (61/459,724) related to this work.

Supporting Online Material

www.sciencemag.org/cgi/content/full/332/6025/81/DC1
Materials and Methods
Figs. S1 to S5
References

30 December 2010; accepted 2 March 2011
10.1126/science.1202357

Thermochronometry Reveals Headward Propagation of Erosion in an Alpine Landscape

David L. Shuster,[1,2]*‡ Kurt M. Cuffey,[3,2]‡ Johnny W. Sanders,[2] Greg Balco[1]

Glacial erosion of mountain ranges produces spectacular alpine landscapes and, by linking climate with tectonics, influences a broad array of geophysical phenomena. Although the resultant landforms are easily identified, the timing and spatial pattern of topographic adjustment to Pleistocene glaciations remain poorly known. We investigated topographic evolution in the archetypal glacial landscape of Fiordland, New Zealand, using (U-Th)/He thermochronometry. We find that erosion during the past 2 million years removed the entire pre-Pleistocene landscape and fundamentally reshaped the topography. Erosion focused on steep valley segments and propagated from trunk valleys toward the heads of drainage basins, a behavior expected if subglacial erosion rate depends on ice sliding velocity. The Fiordland landscape illustrates complex effects of climate on Earth's surface morphology.

The characteristic landforms and large relief of many alpine landscapes indicate that the effect of glacial erosion over the past ~2.5 million years (My) has been profound (*1*, *2*). Understanding how this erosion progressed at the landscape scale over millions of years is essential for analyzing the connections between climate change, topography, and tectonic processes. Most quantitative studies of glacial landscape evolution rely on model simulations that calculate glacial erosion from poorly validated parameterizations [e.g., (*3*, *4*)]. Alternatively, direct observational constraints could reveal the evolution of topography and so guide model development [e.g., (*5*–*7*)]. Such constraints are difficult to obtain, however, because erosion itself effaces evidence of past topography.

We used the isotopic legacy of evolving crustal temperature conditions to constrain the history of relief development in a mountain landscape. We collected low-temperature thermochronometric measurements of 33 bedrock samples from along valley axes and up valley walls in high-relief drainage networks near Milford Sound in Fiordland, New Zealand (*8*). In this setting, patterns of topographic evolution over the past ~2 My are clearly decipherable because of a fortuitous correspondence between the temperature sensitivity of He isotopic techniques and the overall magnitude of Pleistocene exhumation. All samples were taken from a ~21-km–by–38-km region (Fig. 1). The valleys exhibit classic glacial forms, including U-shaped cross sections, concave longitudinal profiles dominated by low slopes, and deeply incised valley-head cirques with exception-

[1]Berkeley Geochronology Center, 2455 Ridge Road, Berkeley, CA 94709, USA. [2]Department of Earth and Planetary Science, University of California, Berkeley, CA 94720, USA. [3]Department of Geography, University of California, Berkeley, CA 94720, USA.

*To whom correspondence should be addressed. E-mail: dshuster@bgc.org
‡These authors contributed equally to this manuscript.